

Hole Selective MoO_x Contact for Silicon Solar Cells

Corsin Battaglia,^{†,‡,∇} Xingtian Yin,^{†,‡,§,∇} Maxwell Zheng,^{†,‡} Ian D. Sharp,^{||} Teresa Chen,[⊥] Stephen McDonnell,[○] Angelica Azcatl,[○] Carlo Carraro,[#] Biwu Ma,[⊥] Roya Maboudian,[#] Robert M. Wallace,[○] and Ali Javey^{*,†,‡}

[†]Electrical Engineering and Computer Sciences Department, University of California, Berkeley, California 94720, United States

[‡]Materials Sciences Division, Lawrence Berkeley National Laboratory, Berkeley, California 94720, United States

[§]Electronic Materials Research Laboratory, Xi'an Jiaotong University, Xi'an, 710049 Shaanxi, People's Republic of China

^{||}Joint Center for Artificial Photosynthesis, Lawrence Berkeley National Laboratory, Berkeley, California 94720, United States

[⊥]Molecular Foundry, Lawrence Berkeley National Laboratory, Berkeley, California 94720, United States

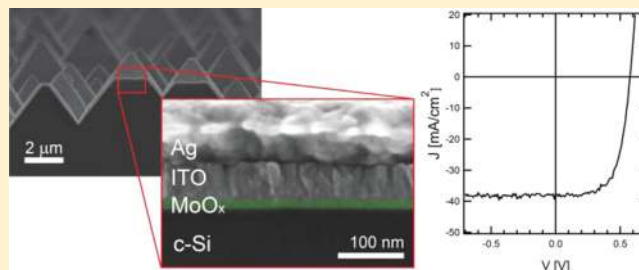
[○]Materials Science and Engineering, University of Texas, Dallas, Texas 75083, United States

[#]Chemical and Biomolecular Engineering, University of California, Berkeley, California 94720, United States

S Supporting Information

ABSTRACT: Using an ultrathin (~15 nm in thickness) molybdenum oxide (MoO_x, $x < 3$) layer as a transparent hole selective contact to n-type silicon, we demonstrate a room-temperature processed oxide/silicon solar cell with a power conversion efficiency of 14.3%. While MoO_x is commonly considered to be a semiconductor with a band gap of 3.3 eV, from X-ray photoelectron spectroscopy we show that MoO_x may be considered to behave as a high workfunction metal with a low density of states at the Fermi level originating from the tail of an oxygen vacancy derived defect band located inside the band gap. Specifically, in the absence of carbon contamination, we measure a work function potential of ~6.6 eV, which is significantly higher than that of all elemental metals. Our results on the archetypical semiconductor silicon demonstrate the use of nm-thick transition metal oxides as a simple and versatile pathway for *dopant-free* contacts to inorganic semiconductors. This work has important implications toward enabling a novel class of junctionless devices with applications for solar cells, light-emitting diodes, photodetectors, and transistors.

KEYWORDS: Junctionless solar cells, silicon photovoltaics, heterojunctions, dopant-free contact, molybdenum trioxide



Hybrid organic/inorganic solar cells combining an organic hole transport layer such as PEDOT:PSS, spiro-OMeTAD, or P3HT with n-type crystalline silicon have generated considerable interest as an alternative to traditional silicon photovoltaics with the potential to reduce cost by adopting room-temperature solution processing.^{1–5} Power conversion efficiencies have been rising steadily over the past three years due to improvements of the organic hole transport materials, interface properties, and light management and have recently reached up to 13%.² However, further efficiency improvements are mandatory to render hybrid solar cells economically viable.

Hybrid organic/silicon devices now routinely achieve open-circuit voltages (V_{oc}) close to 600 mV, and focus has moved toward exploring various nanotexturing schemes, including metal-assisted chemical etching and reactive ion etching, to improve the short-circuit current density (J_{sc}).^{1–3} However, nanotexturing often leads to difficulties with conformal coating of the organic hole contact.^{2,4,5} In addition, the air and ultraviolet stability of polymers remains a major concern.^{6,7}

Here we introduce a solar cell architecture using a transparent substoichiometric molybdenum trioxide (MoO_x, $x < 3$) with a sub-100 nm thickness as a hole-selective, dopant-free contact to n-type silicon. Transition metal oxides have been studied extensively as hole contacts for organic solar cells, organic light emitting diodes, and organic thin film transistors and have led to significant improvements in device performance and stability.^{8–18} To our surprise, transition metal oxides have not yet been employed in conjunction with n-type silicon absorbers. In this work, we demonstrate a room-temperature processed MoO_x/silicon solar cell with a V_{oc} of 580 mV implementing an industrially proven silicon pyramid texture for maximum light absorption reaching an efficiency of 14.3%. Using X-ray photoelectron spectroscopy (XPS), we further demonstrate that much of the controversy around the band alignment and electronic behavior of MoO_x^{8,9} can be resolved by interpreting

Received: November 26, 2013

Revised: December 24, 2013

Published: January 7, 2014

MoO_x as a high workfunction metal with a low density of states at the Fermi level originating from a defect band inside the band gap.

MoO_x thin films with a thickness of 40 nm were thermally evaporated onto flat n-type silicon (100) substrates with a carrier concentration of 10¹⁵ cm⁻³ from stoichiometric MoO₃ powder at a rate of 0.5 Å/s from an Al₂O₃ coated W boat at a pressure in the mid 10⁻⁶ mbar range. The Al₂O₃ coating is important to guarantee a controlled evaporation rate. The substrates were etched in hydrofluoric acid right before loading into the evaporator. The electronic band structure was characterized via XPS using monochromated Al K_α X-rays with a photon energy of 1486.7 eV at a pressure in the low 10⁻⁹ to mid 10⁻¹⁰ mbar range. To study the valence band region and workfunction of MoO_x, Al K_α photons were chosen over the more conventional He I line with 21.2 eV radiation in order to benefit from the longer inelastic mean free path of photoelectrons resulting in increased probing depth (5–10 nm judging from the visibility of Si 2p photoelectrons from the silicon substrate) and consequently enhanced bulk sensitivity.

In order to correctly interpret the electronic structure of evaporated MoO_x films it is important to understand their atomic structure. The MoO₃ single crystal structure is schematically shown in Figure 1a. Each Mo atom is surrounded by six octahedrally coordinated O atoms arranged into intertwined double layers which are stacked via van der Waals forces. One vertex of each octahedron extends into the van der Waals gaps,

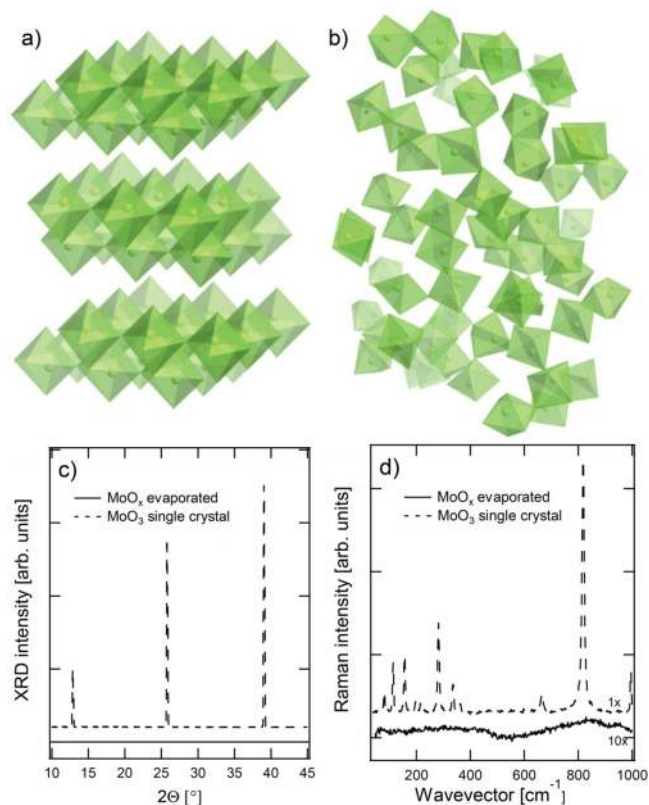


Figure 1. Sketch of the (a) crystalline and (b) amorphous atomic structure of MoO_x. (c) XRD and (d) Raman spectra. For Raman measurements MoO_x was evaporated on a 100 nm thick sputtered Ag film on silicon. Elemental Ag shows no Raman signal as the face-centered cubic unit cell with only one atom supports acoustic phonons only, but no (Raman active) optical phonons.

two vertices are shared with two neighboring octahedra, and the remaining three vertices are shared with three neighboring octahedra (octahedra joined by edges), resulting in an effective total of three O atoms per Mo atom.

Figure 1c and d show X-ray diffraction and Raman scattering data of a MoO₃ single crystal, grown by heating MoO₃ powder to 800 °C in a quartz tube furnace, while flowing O₂/Ar = 20%:80%, indicating sharp diffraction peaks and vibrational modes respectively. No such peaks are observed for the evaporated MoO_x thin films, pointing toward an amorphous structure as shown in Figure 1b. An earlier X-ray absorption fine structure investigation¹⁹ confirms that evaporated MoO_x films retain the local octahedral coordination of the Mo cation, but confirms the absence of long-range order. In addition, octahedra in amorphous films are predominantly connected via vertices (not edges) to their six neighboring octahedra, resulting in a total of three O atoms per Mo cation.

We now focus on the implications of the amorphous structure on the valence or oxidation state of the Mo ions. The bottom curve in Figure 2a presents the photoelectron spectrum of the

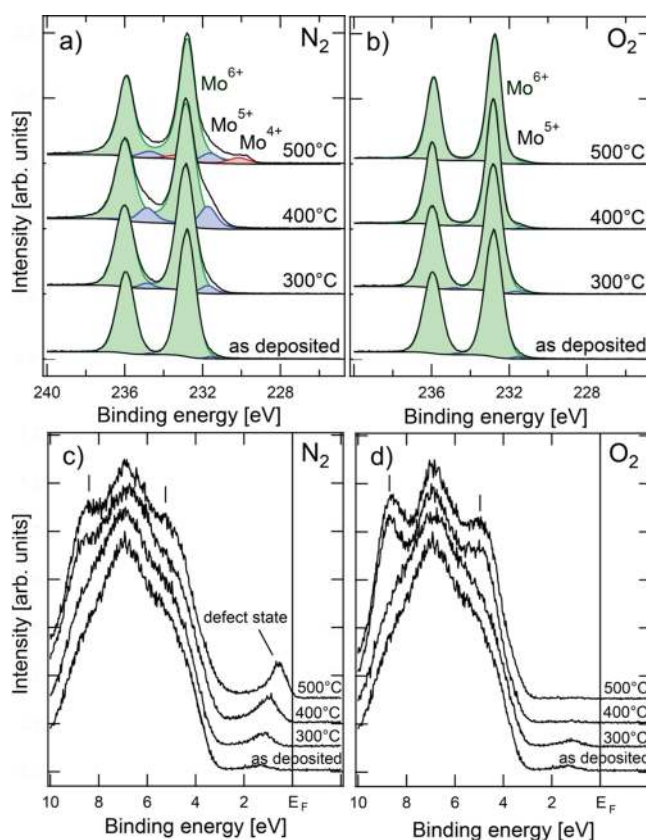


Figure 2. Effect of 30 s rapid thermal annealing in N₂ or O₂ ambient on the Mo 3d core level (a and b) and valence band region (c and d) of evaporated MoO_x films. In (a) and (b) the individual fitted components are shown in color along with a Shirley background.

Mo 3d core level of the evaporated MoO_x film. The core level is split into the 3d_{5/2} and 3d_{3/2} doublet centered at 232.8 and 236.0 eV, respectively, in good agreement with previous work.²⁰ We identify these two main components with the fully oxidized Mo⁶⁺ valence state corresponding to an intact octahedral coordination consisting of six O atoms.

To obtain a satisfactory fit to the experimental XPS data, a second doublet at lower binding energy is required, which we

identify as the Mo^{5+} valence state, corresponding to an oxygen vacancy at the vertex of an octahedron in the amorphous network. As the nearest neighbor correlation is preserved in the amorphous octahedron network, this reduced Mo state is expected to exhibit a relatively well-defined center energy smeared out to second order by the variations in local bond lengths and angles caused by the amorphous environment.

The valence state of the Mo cations can be reduced further by rapid thermal annealing in ambient N_2 as demonstrated in the stacked spectra in Figure 2a. With increasing annealing temperature the intensity of the Mo^{5+} state increases significantly, which is consistent with the creation of additional oxygen vacancies. After annealing at 500°C , we observe an additional shoulder in the Mo $3d$ core level at an even lower binding energy, which we identify as the Mo^{4+} valence state corresponding to an octahedron with two missing O atoms. The formation of oxygen vacancies is reversible by annealing the amorphous MoO_x network in ambient O_2 leading to a suppression of the Mo^{5+} and Mo^{4+} states as can be seen from Figure 2b. Annealing at high temperature leads to a partial crystallization of the MoO_x films as witnessed by Raman spectroscopy (not shown), which can be avoided by reduction or oxidation at room temperature in atomic hydrogen or ozone environment respectively.

We now turn to the discussion of the valence band spectrum of the MoO_x films shown in Figure 2c and d. The valence band spectra, which were also acquired using Al K_α photons, are dominated by the mostly O $2p$ derived bands extending from 3.2 eV to a higher binding energy. The edge of this O $2p$ derived band does not shift appreciably upon creation or annihilation of oxygen vacancies indicating that oxygen vacancies are not acting as shallow level donors in MoO_x . Of particular interest is the small defect band in the band gap visible in the as-deposited film at a binding energy of 1 eV. While this band has already been observed in early photoemission studies,²⁰ it has remained a source of controversy⁸ concerning its implication on band alignment and charge transport in organic devices. Its spectral weight increases with increasing annealing temperature in N_2 (Figure 2c) and can be completely suppressed via annealing in ambient O_2 (Figure 2d).

Similar modifications of the valence band structure can be obtained through atomic hydrogen or ozone exposure avoiding the formation of the two shoulders in the O $2p$ valence band at binding energies of 5 and 9 eV (marked by the short vertical lines in Figure 2c and d) resulting from partial crystallization. These results are clear evidence that the defect band derives from the oxygen vacancies in the octahedron network; i.e. it is associated with Mo $4d$ electrons which remain loosely bound to the Mo atoms.

With increasing annealing temperature in N_2 , we further observe a broadening and a shift of the center of the defect band toward the Fermi energy (E_F) at zero binding energy to a point where the band gap is completely filled up to the Fermi level. It is interesting to note that while fully stoichiometric MoO_3 with only Mo^{6+} is insulating, MoO_2 with only Mo^{4+} is known to be metallic and exhibits an unambiguous metallic Fermi-Dirac edge at zero binding energy.²⁰ As the detection limit for XPS is in the 1% atomic ratio range, we hypothesize that a small but finite density of states at the Fermi level below the detection limit of XPS is also present for the as-deposited MoO_x film, even if the apparent defect density is much lower.

To strengthen our hypothesis, we compare in Figure 3a XPS valence spectra of evaporated MoO_x before and after annealing at

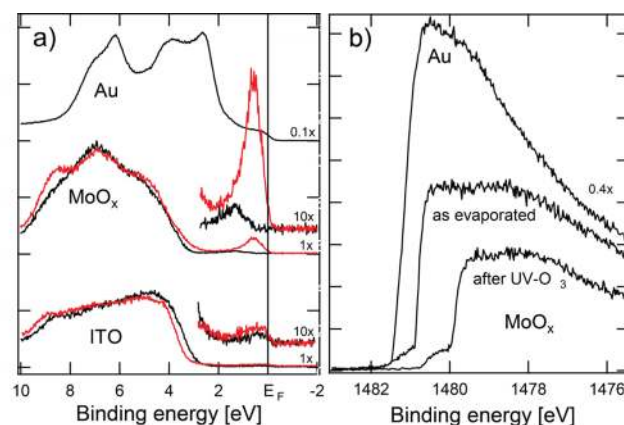


Figure 3. (a) Comparison of density of states at the Fermi level for ITO, MoO_x , and Au reference. The as-deposited MoO_x film is shown in black, and the N_2 annealed film, in red. The ITO with 10^{21} and 10^{20} cm^{-3} electrons are shown in red and black respectively. (b) Secondary electron cutoff for MoO_x and Au reference. The intensity at the high binding energy side of the steep cutoff is due to an analyzer specific artifact. The evaporated MoO_x film was exposed to UV-ozone (UV-O_3) to increase the workfunction by removal of adventitious carbon at the surface.

500°C in N_2 with valence spectra of indium tin oxide (ITO) ($\text{In}_2\text{O}_3/\text{SnO}_2 = 90\%:10\%$). The ITO films were sputtered without and with oxygen in the argon plasma to tune the electron concentration to 10^{21} and 10^{20} cm^{-3} , respectively, as measured by the Hall effect. The region near the Fermi level for each spectrum is replotted with a scaling factor of 10 to allow easier comparison. The spectrum of a gold reference exhibiting a clear Fermi-Dirac step is also shown with a scaling factor of 0.1. While a metallic Fermi-Dirac edge of the ITO samples, already observed in ref 21 falls just within the detection limit of XPS, we do not observe any appreciable spectral weight at the Fermi level of the as-deposited MoO_x films. Consequently we argue that spectral weight at the Fermi level corresponding to a Hall carrier density in the lower 10^{19} cm^{-3} range or below cannot be detected by standard XPS. However, after annealing in N_2 at 500°C , a significant density of states at the Fermi level of MoO_x becomes apparent indicating metallic behavior, which we attribute to the appearance of Mo^{4+} ions. Thus it is reasonable to assume that minute amounts of Mo^{4+} ions are already present in the evaporated film and can cause metallic behavior.

For the ITO samples, the shift of the valence band maximum toward higher binding energy confirms that the Fermi level moves deeper into the conduction band with increasing carrier density. The creation of oxygen vacancies therefore dopes ITO with electrons. Interestingly such a shift is not observed for MoO_x as a function of defect level intensity, indicating that the Fermi level does not move within the MoO_3 host when oxygen vacancies are created. Instead the band gap becomes filled with additional Mo $4d$ states.

Figure 3b shows secondary electron cut-offs of the photoelectron spectra, from which we extract the workfunction by extrapolating the linear part of the cutoff to zero intensity and subtracting this energy from the Al K_α X-ray excitation energy of 1486.7 eV (the spectra are corrected for an externally applied bias of -9.87 V on the sample, which accelerates photoelectrons away from the sample into the detector). The workfunction for the Au reference sputter cleaned in vacuo is 5.1 eV, in good agreement with values found in literature.²² For the evaporated MoO_x film transferred in air to the XPS chamber we obtain 5.7 eV. It is well-

known that the workfunction of MoO_x is very sensitive to air exposure.⁸ To explore the workfunction potential of evaporated MoO_x , we exposed the films to UV-ozone (UV-O_3) at 900 mbar for 30 min. From XPS, we see a reduction of adventitious carbon contamination (not shown)²³ and a dramatic increase of the workfunction to a value as high as 6.6 eV even with some residual C 1s signal. The same value was obtained after a prolonged 6 h exposure resulting in complete elimination of the C 1s signal below the detection limit. This clearly demonstrates the high workfunction and consequently electron affinity potential of MoO_x exceeding those of elemental metals²⁴ and confirms earlier work on in situ evaporated MoO_x .²⁵ Even with slight carbon contamination, the workfunction remains sufficiently high to bring the Fermi level of MoO_x close to the position of the valence band maximum of silicon located at 5.1 eV. MoO_x can thus be used as a selective contact for a MoO_x /silicon solar cell.

Solar cells were fabricated by deposition of a 15 nm thick MoO_x layer on a potassium hydroxide (KOH) textured silicon wafer right after removal of the native oxide in dilute hydrofluoric (HF) acid (see Figure 4a and b). After air exposure, the MoO_x

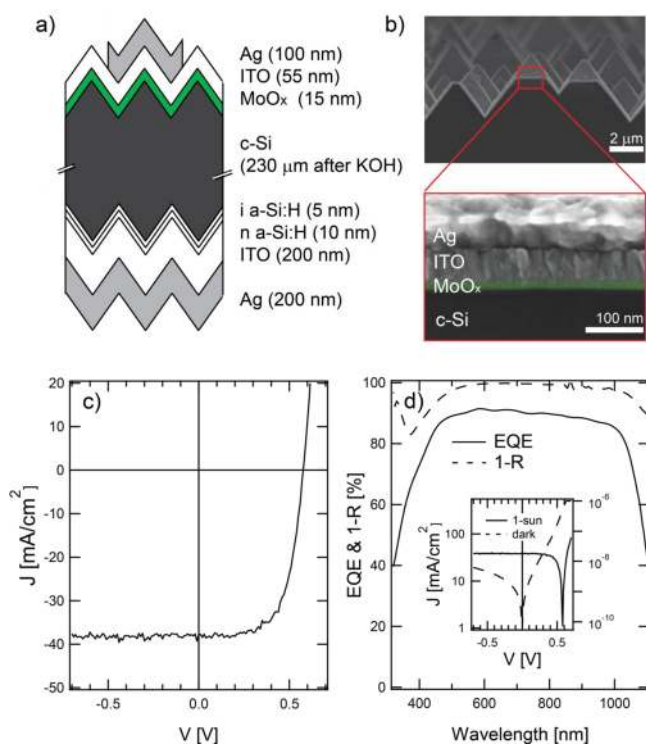


Figure 4. (a) Schematics of the MoO_x /n-Si heterojunction solar cell structure with (b) false-colored cross section imaged by scanning electron microscopy, (c) J - V and (d) EQE and $1-R$ curve. The inset in (d) shows dark (right scale) and light (left scale) J - V curves in logarithmic scales. Pyramids in (a) are not drawn to scale and are not necessarily commensurate on front and back side.

layer was covered with 55 nm of sputtered ITO deposited in an Ar plasma at 10^{-2} mbar and an evaporated 100 nm thick Ag grid with a finger width of 11 μm and pitch of 490 μm was patterned via photolithography and lift-off. We chose a hydrogenated amorphous silicon passivated ITO/Ag back contact capable of open-circuit voltages of up to 720 mV²⁶ in order to study the open-circuit voltage potential of the MoO_x /Si frontside heterojunction interface with minimum recombination at the

backside. The finalized cells were annealed at 150 °C in N_2 for 10 min to improve the conductivity of the ITO electrode.²⁷

Figure 4c presents the J - V curves for solar cells patterned and masked to an area of 5 mm \times 5 mm and measured under standard test conditions (1000 W/m^2 , air mass 1.5 global (AM1.5_g) spectrum and 25 °C). With an open-circuit voltage (V_{oc}) of 580 mV, a short-circuit current (J_{sc}) of 37.8 mA/cm^2 (including 2% grid shading) and a fill factor (FF) of 65%, a power conversion efficiency of 14.3% is obtained. The external quantum efficiency (EQE) and reflectance (R , presented as $1 - R$, measured with an integrating sphere) are shown in Figure 4d along with the dark and light J - V curves in a semilogarithmic plot in the inset.

While our simple cell design with the unpassivated MoO_x /silicon interface cannot rival the performance of state-of-the-art silicon heterojunction solar cells, which integrate a sophisticated amorphous silicon passivation scheme,¹⁸ it clearly illustrates the concept of a transparent dopant-free selective hole contact to n-type silicon. With a demonstrated V_{oc} potential of 580 mV, our MoO_x /silicon solar cell nevertheless reaches values that are as high as those for the best-in-class hybrid organic/silicon solar cells (see Table S1). A significantly higher J_{sc} is obtained due to the traditional pyramid texture in conjunction with a carefully optimized oxide layer thickness (see Supporting Information for more details) for minimum reflection losses which outperforms nanotextures obtained by metal-assisted etching or reactive ion etching. MoO_x /silicon consequently reaches an efficiency higher than that of hybrid organic/silicon solar cells.

Various potential improvements of our cell design can be envisioned including the implementation of a passivation layer with local MoO_x contact openings or the addition of an intrinsic amorphous silicon passivation layer in conjunction with a MoO_x contact to improve V_{oc} . The FF could be improved by optimizing the defect state density in the band gap of MoO_x or by depositing an ultrathin highly conformal MoO_x layer by atomic layer deposition. A higher J_{sc} could be achieved by improving the ITO transparency and reducing shadowing due to the Ag finger grid. MoO_x could also be replaced by other transition metal oxides such as NiO_x , VO_x , or WO_x which have proven to function as hole contacts in organic electronics.⁸ Furthermore MoO_x along with ITO and other transparent conductive oxides were shown to be compatible with solution processing^{11,13,27} enabling a route toward a low-cost, fully solution-processed cell architecture.

In conclusion, we demonstrated a simple MoO_x /silicon solar cell with an efficiency of 14.3%. With a high workfunction exceeding those of elemental metals, MoO_x presents an important opportunity for hole contact in not only inorganic semiconductor materials with low lying valence band maxima including III-V semiconductors such as InP or GaN but also layered transition metal dichalcogenide semiconductors as well as oxide- and carbon-based nanomaterials.

■ ASSOCIATED CONTENT

Supporting Information

Compilation of hybrid organic/silicon solar cell performance characteristics. Optimization of ITO/ MoO_x thicknesses. This material is available free of charge via the Internet at <http://pubs.acs.org>.

■ AUTHOR INFORMATION

Corresponding Author

*E-mail: ajavey@eecs.berkeley.edu.

Author Contributions

▽ Authors with equal contribution.

Notes

The authors declare no competing financial interest.

ACKNOWLEDGMENTS

MoO_x processing and characterization were funded by the Center for Low Energy Systems Technology (LEAST), one of the six SRC STARnet centers sponsored by MARCO and DARPA. Photovoltaic device fabrication and characterization were funded by the Bay Area Photovoltaics Consortium (BAPVC). Some of the XPS measurements were performed at JCAP; this material is based upon work performed by the Joint Center for Artificial Photosynthesis, a DOE Energy Innovation Hub, supported through the Office of Science of the U.S. Department of Energy under Award Number DE-SC0004993. We thank L. Barraud, S. De Wolf, and C. Ballif from the Ecole Polytechnique Federale de Lausanne (EPFL) for providing textured silicon wafers with passivated back contacts. C.B. acknowledges support from the Zeno Karl Schindler Foundation. A.J. acknowledges support from the BK21 Plus program at Suncheon National University.

REFERENCES

- (1) See Table S1 for a compilation of device performance characteristics
- (2) Yu, P.; Tsai, C.-Y.; Chang, J.-K.; Lai, C.-C.; Chen, P.-H.; Lai, Y.-C.; Tsai, P.-T.; Li, M.-C.; Pan, H.-T.; Huang, Y.-Y.; Wu, C.-I.; Chueh, Y.-L.; Chen, S.-W.; Du, C.-H.; Horng, S.-F.; Meng, H.-F. 13% Efficiency Hybrid Organic/Silicon-Nanowire Heterojunction Solar Cell via Interface Engineering. *ACS Nano* **2013**, *7*, 10780.
- (3) Jeong, S.; Garnett, E. C.; Wang, S.; Yu, Z.; Fan, S.; Brongersma, M. L.; McGehee, M. D.; Cui, Y. Hybrid Silicon Nanocone-polymer Solar Cells. *Nano Lett.* **2012**, *12*, 2971.
- (4) He, L.; Jiang, C.; Rusli, D.; Wang, H. Highly efficient Si-nanorods/organic hybrid core-sheath heterojunction solar cells. *Appl. Phys. Lett.* **2011**, *99*, 021104.
- (5) Chen, T. G.; Huang, B. Y.; Chen, E. C.; Yu, P. C.; Meng, H. F. Micro-textured conductive polymer/silicon heterojunction photovoltaic devices with high efficiency. *Appl. Phys. Lett.* **2012**, *101*, 033301.
- (6) Jorgensen, M.; Norman, K.; Krebs, F. C. Stability/degradation of polymer solar cells. *Sol. Energy Mater. Sol. Cells* **2008**, *92*, 686–714.
- (7) Reese, M. O.; Gevorgyan, S. A.; Jorgensen, M.; Bundgaard, E.; Kurtz, S. R.; et al. Consensus stability testing protocols for organic photovoltaic materials and devices. *Sol. Energy Mater. Sol. Cells* **2011**, *95*, 1253–1267.
- (8) Meyer, J.; Hamwi, S.; Kröger, M.; Kowalsky, W.; Riedl, T.; Kahn, A. Transition Metal Oxides for Organic Electronics: Energetics, Device Physics and Applications. *Adv. Mater.* **2012**, *24*, 5408–5427.
- (9) Greiner, M. T.; Helander, M. G.; Tang, W.-M.; Wang, Z.-B.; Qiu, J.; Lu, Z.-H. Universal energy-level alignment of molecules on metal oxides. *Nat. Mater.* **2012**, *11*, 76.
- (10) Papadopoulos T. A.; Meyer J.; Li H.; Guan Z.; Kahn A.; Brédas J.-L. Nature of the Interfaces Between Stoichiometric and Under-Stoichiometric MoO₃ and 4,4-N,N'-dicarbazole-biphenyl: A Combined Theoretical and Experimental Study, *Adv. Funct. Mater.*, early online view DOI: 10.1002/adfm.201301466.
- (11) Murase, S.; Yang, Y. Solution Processed MoO₃ Interfacial Layer for Organic Photovoltaics Prepared by a Facile Synthesis Method. *Adv. Mater.* **2012**, *24*, 2459.
- (12) Sun, Y.; Takacs, C. J.; Cowan, S. R.; Seo, J. W.; Gong, X.; Roy, A.; Heeger, A. J. Efficient, Air-Stable Bulk Heterojunction Polymer Solar Cells Using MoO_x as the Anode Interfacial Layer. *Adv. Mater.* **2011**, *23*, 2226–2230.
- (13) Stubhan, T.; Ameri, T.; Salinas, M.; Krantz, J.; Machui, F.; Halik, M.; Brabec, C. J. High shunt resistance in polymer solar cells comprising

a MoO₃ hole extraction layer processed from nanoparticle suspension. *Appl. Phys. Lett.* **2011**, *98*, 253308.

(14) Kröger, M.; Hamwi, S.; Meyer, J.; Riedl, T.; Kowalsky, W.; Kahn, A. Role of deep-lying electronic states of MoO₃ in the enhancement of hole-injection in organic thin films. *Appl. Phys. Lett.* **2009**, *95*, 123301.

(15) Lee, H.; Cho, S. W.; Han, K.; Jeon, P. E.; Whang, C.-M.; Jeong, K.; Cho, K.; Yi, Y. The origin of hole injection improvements at the indium tin oxide/molybdenum trioxide/N,N'-bis(1-naphthyl)-N,N'-diphenyl-1,1'-biphenyl-4,4'-diamine interfaces. *Appl. Phys. Lett.* **2008**, *93*, 043308.

(16) Kanno, H.; Holmes, R. J.; Sun, Y.; Kena-Cohen, S.; Forrest, S. R. White Stacked Electrophosphorescent Organic Light-Emitting Devices Employing MoO₃ as a Charge-Generation Layer. *Adv. Mater.* **2006**, *18*, 339.

(17) Chu, C.-W.; Li, S.-H.; Chen, C.-W.; Shrotriya, V.; Yang, Y. High-performance organic thin-film transistors with metal oxide/metal bilayer electrode. *Appl. Phys. Lett.* **2005**, *87*, 193508.

(18) Tokito, S.; Noda, K.; Taga, Y. Metal oxides as hole-injection layer for an organic electroluminescent device. *J. Phys. D: Appl. Phys.* **1996**, *29*, 2750–2753.

(19) Burattini, E. XAFS Studies of Octahedral Amorphous Oxides. *Jpn. J. Appl. Phys.* **1993**, *32*, 655–657.

(20) Werfel, F.; Minni, E. Photoemission study of the electronic structure of Mo and Mo oxides. *J. Phys. C: Solid State Phys.* **1983**, *16*, 6091–6100.

(21) Walsh, A.; Da Silva, J. L. F.; Wei, S.-H.; Körber, C.; Klein, A.; Piper, L. F. J.; DeMasi, A.; Smith, K. E.; Panaccione, G.; Torelli, P.; Payne, D. J.; Bourlange, A.; Egdell, R. G. Nature of the band gap in In₂O₃ by first-principles calculations and X-ray spectroscopy. *Phys. Rev. Lett.* **2008**, *100*, 167402.

(22) Baer, Y. The natural energy scale for XPS spectra of metals. *Sol. State. Comm.* **1976**, *19*, 669–671.

(23) Barr, T. L.; Seal, S. Nature of the use of adventitious carbon as binding energy standard. *J. Vac. Sci. Technol. A* **1995**, *13*, 1239.

(24) Michaelson, H. B. The work function of the elements and its periodicity. *J. Appl. Phys.* **1977**, *48*, 4729.

(25) Meyer, J.; Shu, A.; Kröger, M.; Kahn, A. Effect of contamination on the electronic structure and hole-injection properties of MoO₃/organic semiconductor interfaces. *Appl. Phys. Lett.* **2010**, *96*, 133308.

(26) Barraud, L.; Holman, Z. C.; Badel, N.; Reiss, P.; Descoeurdes, A.; Battaglia, C.; De Wolf, S.; Ballif, C. Hydrogen-doped indium oxide/indium tin oxide bilayers for high-efficiency silicon heterojunction solar cells. *Sol. Energy Mater. Sol. Cells* **2013**, *115*, 151–156.

(27) Battaglia, C.; Erni, L.; Boccard, M.; Barraud, L.; Escarré, J.; Söderström, K.; Bugnon, G.; Billet, A.; Ding, L.; Despeisse, M.; Haug, F.-J.; De Wolf, S.; Ballif, C. Micromorph thin-film silicon solar cells with transparent high-mobility hydrogenated indium oxide front electrodes. *J. Appl. Phys.* **2011**, *109*, 114501.

(28) Pasquarelli, R. M.; Ginley, D. S.; O'Hayre, R. Solution processing of transparent conductors: from flask to film. *Chem. Soc. Rev.* **2011**, *40*, 5406–5441.

Hole selective MoO_x contact for silicon solar cells

Corsin Battaglia^{1,2,#}, Xingtian Yin^{1,2,3,#}, Maxwell Zheng^{1,2}, Ian D. Sharp⁴, Teresa Chen⁵, Stephen McDonnell⁶, Angelica Azcatl⁶, Carlo Carraro⁷, Roya Maboudian⁷, Robert. M. Wallace⁶ and Ali Javey^{1,2,*}

¹*Electrical Engineering and Computer Sciences Department, University of California, Berkeley, CA 94720*

²*Materials Sciences Division, Lawrence Berkeley National Laboratory, Berkeley, CA 94720*

³*Electronic Materials Research Laboratory, Xi'an Jiaotong University, Xi'an, 710049 Shaanxi, People's Republic of China*

⁴*Joint Center for Artificial Photosynthesis, Lawrence Berkeley National Laboratory, Berkeley, CA 94720*

⁵*Molecular Foundry, Lawrence Berkeley National Laboratory, Berkeley, CA 94720*

⁶*Materials Science and Engineering, University of Texas, Dallas, TX 75083*

⁷*Chemical and Biomolecular Engineering, University of California, Berkeley, CA 94720*

#Authors with equal contribution

*Corresponding Author: ajavey@eecs.berkeley.edu

Supporting information

Table S1: Compilation of hybrid organic/silicon solar cell performance characteristics, also included are results for graphene/silicon and carbon nanotubes/silicon solar cells.

Reference	Hole contact	Texture	V _{oc} [mV]	J _{sc} [mA/cm ²]	FF [%]	Efficiency [%]
This work	MoO _x /ITO	KOH	580	37.8	65.0	14.3
Yu et al., ACS Nano, 2013 [1]	TAPC/PEDOT:PSS	AgNO ₃ +HF	540	34.8	69.5	13.0
Nagamatsu et al., IEEE JPV 2013 [2]	PEDOT :PSS	None	570	27.8	73.0	11.7
Wei et al., Nano Lett., 2013 [3]	PEDOT:PSS	KOH/Au +H ₂ O ₂ +HF	520	34.5	64.1	11.5
Liu et al., Appl. Phys. Lett., 2012 [4]	PEDOT:PSS	None	541	29.2	71.8	11.3
Jung et al., Nano Lett., 2012 [5]	Carbon nanotubes	None	530	28.6	74.1	11.2
Jeong et al., Nano Lett. 2012 [6]	PEDOT:PSS	RIE	550	29.6	67.7	11.1
Ono et al., Appl. Phys. Exp., 2012 [7]	Graphene/PEDOT:PSS	none	548	28.9	67.5	10.7
He et al., Appl. Phys. Lett., 2012 [8]	PEDOT:PSS	none	610	26.4	65.9	10.6
He, Appl. Phys. Lett., 2011 [9]	Spiro-OMeTAD/PEDOT:PSS	AgNO ₃ +HF	570	30.9	58.8	10.3
Zhang et al., J. Mat. Chem. A, 2013 [10]	Graphene	AgNO ₃ +HF	552	38.86	48.0	10.3
Avasthi et al., Adv. Mat., 2011 [11]	P3HT/PEDOT:PSS	None	590	29	59.0	10.1
He et al., ACS Appl. Mater. Inter., 2012 [12]	Spiro-OMeTAD/PEDOT:PSS	AgNO ₃ +HF	570	30.7	56.6	9.9
Zhu et al., Appl. Phys. Lett., 2013 [13]	PEDOT:PSS/PFI	None	560	25.3	70.0	9.9
Chen et al., Appl. Phys. Lett., 2012 [14]	PEDOT:PSS	KOH	520	30.4	62.1	9.8

Shen et al., JACS, 2011 [15]	Spiro-OMeTAD/PEDOT:PSS	AgNO ₃ +HF	527	31.3	58.8	9.7
Zhang et al., J. Mat. Chem., 2012 [16]	P3HT/PEDOT:PSS	AgNO ₃ +HF	457	37.6	54	9.2
He et al., IEEE Electron Device Lett., 2011 [17]	PEDOT:PSS	AgNO ₃ +HF	530	26.3	64.2	9.0
Zhang et al., Appl. Phys. Lett., 2013 [18]	PEDOT:PSS	AgNO ₃ +HF	500	29.8	58	8.7
Syu et al., Sol. Energy Mat. & Sol. Cells, 2012 [19]	PEDOT:PSS	AgNO ₃ +HF	532	24.2	65.1	8.4
Zhang et al., Nanotechnology 2012 [20]	PEDOT:PSS	AgNO ₃ +HF	497	30.7	48	7.3
Lu et al., Nanoscale, 2011 [21]	PEDOT:PSS	AgNO ₃ +HF	460	21.6	64	6.4
Cui et al., J. Mat. Chem. A, 2013 [22]	Graphene	none	548	17.9	60.6	6.0
Zhang et al., Chem. Mat. 2013 [23]	P3HT/PEDOT:PSS	AgNO ₃ +HF	421	26.2	53	5.9
He et al., Appl. Phys. Lett., 2012 [24]	PEDOT:PSS	AgNO ₃ +HF	570	13.6	71.9	5.6
Feng et al., Nanoscale 2012 [25]	Graphene/ HNO ₃	ICP	495	17.22	51	4.4
Liu et al., Nanoscale Res. Lett., 2013 [26]	PEDOT:PSPS	AgNO ₃ +HF	455	16.6	42.9	3.2
Tsai et al., ACS Nano, 2011, [27]	P3HT	AgNO ₃ +HF	346	18.9	35.2	2.3
Li et al., Adv Mater., 2010 [28]	Graphene	none	420~480	4~6.5	45~56	1~1.7

Optimization of MoO_x/ITO thicknesses

The front reflectance of a cell with a double layer antireflection coating is giving by the following expression [29]:

$$R=A/B$$

where

$$A= r_1^2+r_2^2+r_3^2+r_1^2 \cdot r_2^2 \cdot r_3^2+2r_1 \cdot r_2(1+r_3^2) \cdot \cos(2 \cdot \theta_1)+2 \cdot r_2 \cdot r_3 \cdot (1+r_1^2) \cdot \cos(2 \cdot \theta_2)+2 \cdot r_1 \cdot r_3 \cdot \cos[2 \cdot (\theta_1+\theta_2)]+2 \cdot r_1 \cdot r_2^2 \cdot r_3 \cdot \cos[2 \cdot (\theta_1-\theta_2)]$$

$$B=1+r_1^2 \cdot r_2^2+r_1^2 \cdot r_3^2+r_2^2 \cdot r_3^2+2 \cdot r_1 \cdot r_2 \cdot (1+r_3^2) \cdot \cos(2 \cdot \theta_1)+2 \cdot r_2 \cdot r_3(1+r_1^2) \cdot \cos(2 \cdot \theta_2)+2 \cdot r_1 \cdot r_3 \cdot \cos[2 \cdot (\theta_1+\theta_2)]+2 \cdot r_1 \cdot r_2^2 \cdot r_3 \cdot \cos[2 \cdot (\theta_1-\theta_2)]$$

with

$$r_1=(n_0-n_1)/(n_0+n_1)$$

$$r_2=(n_1-n_2)/(n_1+n_2)$$

$$r_3=(n_2-n_3)/(n_2+n_3)$$

$$\theta_1=(2 \cdot \pi \cdot n_1 \cdot t_1/\lambda)$$

$$\theta_2=(2 \cdot \pi \cdot n_2 \cdot t_2/\lambda)$$

n_1 , n_2 , n_3 are the refractive indices of ITO, MoO_x and Si in our case, t_1 and t_2 the ITO and MoO_x thicknesses and λ the wavelength. The refractive indices of ITO and MoO_x are almost identical, so that we can assume that $r_2 \approx 0$. In this case, A and B simplify to

$$A= r_1^2 + r_3^2 + 2 \cdot r_1 \cdot r_3 \cdot \cos[2 \cdot (\theta_1 + \theta_2)]$$

$$B=1 + r_1^2 \cdot r_3^2 + 2 \cdot r_1 \cdot r_3 \cdot \cos[2 \cdot (\theta_1 + \theta_2)]$$

From R, we can determine the absorbance $A=1-R$. Convolution of A with the global air mass 1.5 spectrum and integration over all wavelength λ , gives an estimation of the maximum achievable short-circuit current density (J_{sc}) assuming no parasitic light absorption, unity carrier collection and total light trapping. Estimated J_{sc} values as a function of the thicknesses of ITO and MoO_x are shown in Fig. S1.

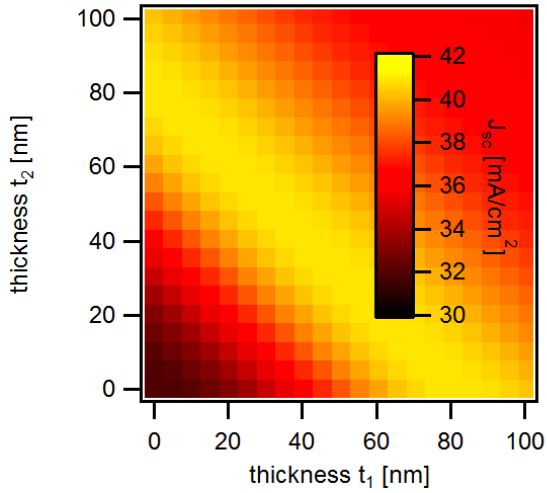


FIG. S1. Estimated J_{sc} values for a flat silicon cell with ITO (t_1) and MoO_x (t_2) layers.

For the pyramidal texture shown in Fig. 4a, most incoming light rays, which are reflected off a first time at a pyramid, hit subsequently a neighboring pyramid and undergo a second reflection event. Thus the effective reflectance of a pyramidally textured surface is given to a first approximation by $R_{\text{pyramid}} = R_{\text{flat}}^2$ [30, 31]. This renders the J_{sc} much more tolerant to variations in layer thicknesses.

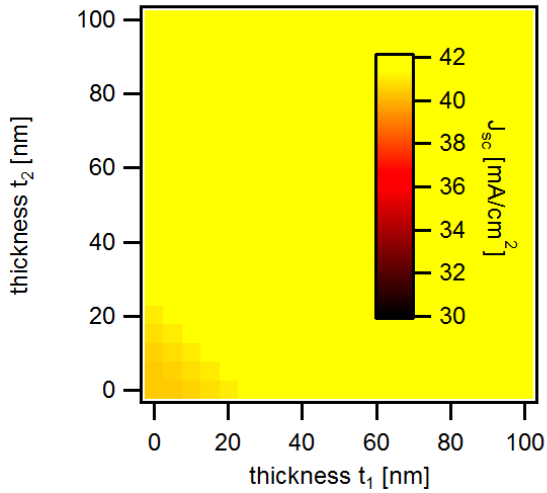


FIG. S2. Estimated J_{sc} values for a pyramidally textured silicon cell with ITO (t_1) and MoO_x (t_2) layers.

Due to the increased surface area of the pyramids compared to the flat surface, the evaporated/sputtered thicknesses of the antireflection layer on the pyramids must be scaled by a factor $1/\cos(54.7^\circ) \approx 1.7$ compared to the flat surface in order to obtain the same effective thickness on the pyramids.

In practice, it is best to optimize the ITO and MoO_x thicknesses directly on flat silicon. Ideally a dark blue color is observed typically at a total oxide thickness of 65 nm to 70 nm (see Fig. S3). The thicknesses are then scaled with a factor of 1.7 and transferred to the pyramid structure.

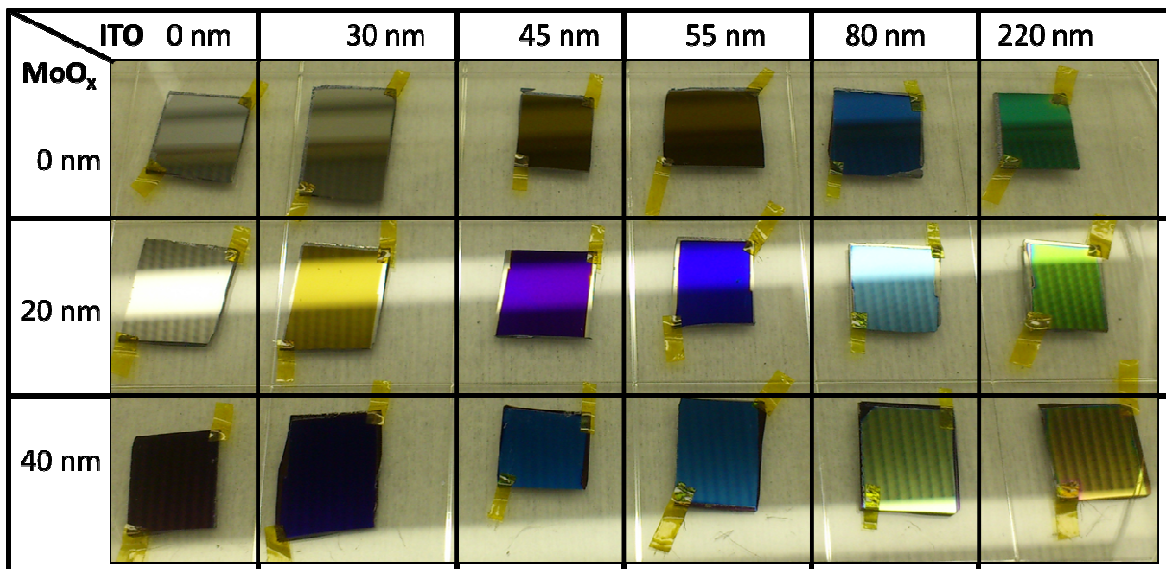


FIG. S3 Optimization of ITO and MoO_x thicknesses on silicon wafer. An ideal dark blue color is observed at 65-70 nm total oxide thickness.

References

- [1]. Yu, P.; Tsai, C.-Y.; Chang, J.-K.; Lai, C.-C.; Chen, P.-H.; Lai, Y.-C.; Tsai, P.-T.; Li, M.-C.; Pan, H.-T.; Huang, Y.-Y.; Wu, C.-I.; Chueh, Y.-L.; Chen, S.-W.; Du, C.-H.; Horng, S.-F.; Meng, H.-F., 13% Efficiency Hybrid Organic/Silicon-Nanowire Heterojunction Solar Cell via Interface Engineering, *ACS Nano* **2013**, 7, 10780.
- [2]. Nagamatsu K. A.; Avasthi S.; Jhaveri J.; Sturm J. C., A 12% Efficient Silicon/PEDOT:PSS Heterojunction Solar Cell Fabricated at $< 100^\circ \text{C}$, *IEEE J. Photovolt.*, **2013**, 4, 260
- [3]. Wei, W.-R.; Tsai, M.-L.; Ho, S.-T.; Tai, S.-H.; Ho, C.-R.; Tsai, S.-H.; Liu, C.-W.; Chung, R.-J.; He, J.-H., Above-11%-Efficiency Organic-inorganic Hybrid Solar Cells with Omnidirectional Harvesting Characteristics by Employing Hierarchical Photon-Trapping Structures, *Nano Lett.* **2013**, 13, 3658.
- [4]. Liu, Q.; Ono, M.; Tang, Z.; Ishikawa, R.; Ueno, K.; Shirai, H., Highly efficient crystalline silicon/Zonyl fluorosurfactant-treated organic heterojunction solar cells, *Appl. Phys. Lett.* **2012**, 100, 183901.
- [5]. Jung, Y.; Li, X.; Rajan, N. K.; Taylor, A. D.; Reed, M. A., Record High Efficiency Single-Walled Carbon Nanotube/Silicon p-n Junction Solar Cells, *Nano Lett.* **2013**, 13, 95.
- [6]. Jeong, S.; Garnett, E. C.; Wang, S.; Yu, Z.; Fan, S.; Brongersma, M. L.; McGehee, M. D.; Cui, Y., Hybrid Silicon Nanocone-polymer Solar Cells, *Nano Lett.* **2012**, 12, 2971.
- [7]. Ono, M.; Tang, Z.; Ishikawa, R.; Gotou, T.; Ueno, K.; Shirai, H., Efficient Crystalline Si/Poly(ethylene dioxythiophene): Poly(styrene sulfonate): Graphene Oxide Composite Heterojunction Solar Cells, *Appl. Phys. Express* **2012**, 5, 032301.
- [8]. He, L.; Jiang, C.; Wang, H.; Lai, D.; Rusli, High efficiency planar Si/organic heterojunction hybrid solar cells, *Appl. Phys. Lett.* **2012**, 100, 073503.
- [9]. He, L.; Jiang, C.; Rusli; Lai, D.; Wang, H., Highly efficient Si-nanorods/organic hybrid core-sheath heterojunction solar cells, *Appl. Phys. Lett.* **2011**, 99, 021104.
- [10]. Zhang, X.; Xie, C.; Jie, J.; Zhang, X.; Wu, Y.; Zhang, W., High-efficiency graphene/Si nanoarray Schottky junction solar cells via surface modification and graphene doping, *J. Mater. Chem. A* **2013**, 1, 6593.

- [11]. Avasthi, S.; Lee, S.; Loo, Y.-L.; Sturm, J. C., Role of Majority and Minority Carrier Barriers Silicon/Organic Hybrid Heterojunction Solar Cells, *Adv. Mater.* **2011**, 23, 5762.
- [12]. He, L.; Jiang, C.; Wang, H.; Lai, D.; Rusli, Si Nanowires Organic Semiconductor Hybrid Heterojunction Solar Cells Toward 10% Efficiency, *ACS Appl. Mater. Interfaces* **2012**, 4, 1704.
- [13]. Zhu, Y.; Song, T.; Zhang, F.; Lee, S.-T.; Sun, B., Efficient organic-inorganic hybrid Schottky solar cell: The role of built-in potential, *Appl. Phys. Lett.* **2013**, 102, 113504.
- [14]. Chen, T. G.; Huang, B. Y.; Chen, E. C.; Yu, P. C.; Meng, H. F., Micro-textured conductive polymer/silicon heterojunction photovoltaic devices with high efficiency, *Appl. Phys. Lett.* **2012**, 101, 033301.
- [15]. Shen, X.; Sun, B.; Liu, D.; Lee, S.-T., Hybrid Heterojunction Solar Cell Based on Organic-inorganic Silicon Nanowire Array Architecture, *J. Am. Chem. Soc.* **2011**, 133, 19408.
- [16]. Zhang, F.; Han, X.; Lee, S.-t.; Sun, B., Heterojunction with organic thin layer for three dimensional high performance hybrid solar cells, *J. Mater. Chem.* **2012**, 22, 5362.
- [17]. Lining, H.; Rusli; Changyun, J.; Hao, W.; Lai, D., Simple Approach of Fabricating High Efficiency Si Nanowire/Conductive Polymer Hybrid Solar Cells, *IEEE Electron Device Lett.* **2011**, 32, 1406.
- [18]. Zhang, J.; Zhang, Y. F.; Zhang, F. T.; Sun, B. Q., Electrical characterization of inorganic-organic hybrid photovoltaic devices based on silicon-poly(3,4-ethylenedioxythiophene):poly(styrenesulfonate), *Appl. Phys. Lett.* **2013**, 102, 013501.
- [19]. Syu, H.-J.; Shiu, S.-C.; Lin, C.-F., Silicon nanowire/organic hybrid solar cell with efficiency of 8.40%, *Sol. Energy Mater. Sol. Cells* **2012**, 98, 267-272.
- [20]. Zhang, F.; Song, T.; Sun, B., Conjugated polymer-silicon nanowire array hybrid Schottky diode for solar cell application, *Nanotechnology* **2012**, 23, 194006.
- [21]. Lu, W.; Wang, C.; Yue, W.; Chen, L., Si/PEDOT:PSS core/shell nanowire arrays for efficient hybrid solar cells, *Nanoscale* **2011**, 3, 3631.
- [22]. Cui, T.; Lv, R.; Huang, Z.-H.; Chen, S.; Zhang, Z.; Gan, X.; Jia, Y.; Li, X.; Wang, K.; Wu, D.; Kang, F., Enhanced efficiency of graphene/silicon heterojunction solar cells by molecular doping, *J. Mater. Chem. A* **2013**, 1, 5736.

- [23]. Zhang, F.; Sun, B.; Song, T.; Zhu, X.; Lee, S., Air Stable, Efficient Hybrid Photovoltaic Devices Based on Poly(3-hexylthiophene) and Silicon Nanostructures, *Chem. Mater.* **2013**, 23, 2084.
- [24]. He, L.; Jiang, C.; Wang, H.; Lai, D.; Heng Tan, Y.; Seng Tan, C.; Rusli, Effects of nanowire texturing on the performance of Si/organic hybrid solar cells fabricated with a 2.2 um thin-film Si absorber, *Appl. Phys. Lett.* **2012**, 100, 103104.
- [25]. Feng, T.; Xie, D.; Lin, Y.; Zhao, H.; Chen, Y.; Tian, H.; Ren, T.; Li, X.; Li, Z.; Wang, K.; Wu, D.; Zhu, H., Efficiency enhancement of graphene/silicon-pillar-array solar cells by HNO₃ and PEDOT-PSS, *Nanoscale* **2012**, 4, 2130.
- [26]. Liu, K.; Qu, S.; Zhang, X.; Tan, F.; Wang, Z., Improved photovoltaic performance of silicon nanowire/organic hybrid solar cells by incorporating silver nanoparticles, *Nanoscale Res. Lett.* **2013**, 8, 88.
- [27]. Tsai, S.-H.; Chang, H.-C.; Wang, H.-H.; Chen, S.-Y.; Lin, C.-A.; Chen, S.-A.; Chueh, Y.-L.; He, J.-H., Significant Efficiency Enhancement of Hybrid Solar Cells Using Core-shell Nanowire Geometry for Energy Harvesting, *ACS Nano* **2011**, 5, 9501.
- [28]. Li, X.; Zhu, H.; Wang, K.; Cao, A.; Wei, J.; Li, C.; Jia, Y.; Li, Z.; Li, X.; Wu, D., Graphene-On-Silicon Schottky Junction Solar Cells, *Adv. Mater.* **2010**, 22, 2743.
- [29] Wang E. Y.; Yu F. T. S.; Sims V. L.; Brandhorst E. W.; Broder J. D., Optimum design of anti-reflection coating for silicon solar cells, *Proc. of the 10th IEEE PVSC* **1973**, 168.
- [30] Campbell P.; Green M. A., Light trapping properties of pyramidally textured surfaces, *J. Appl. Phys.* **1987**, 62, 243.
- [31] Escarré J.; Soederstroem K.; Despeisse M.; Nicolay S.; Battaglia C.; Bugnon G.; Ding L.; Meillaud F.; Haug F.-J.; Ballif C., Geometric light trapping for high efficiency thin film silicon solar cells, *Sol. Ene. Mater. Sol. Cells* **2012**, 98, 185